Preprint

A Machine Learning Strategy for Modelling and Optimal Design of Near-Field Radiative Heat Transfer

Shizheng Wen,[1, a)] Chunzhuo Dang,[1, a)] and Xianglei Liu[1]
School of Energy and Power Engineering, Nanjing University of Aeronautics and Astronautics, Nanjing 210016, China

(*Electronic mail: xliu@nuaa.edu.cn)

(Dated: 27 July 2022)

The past decade has witnessed the advent of near-field radiative heat transfer (NFRHT) in a wide range of applications, including thermal photovoltaics and thermal diodes. However, the design process for these thermal devices has remained complex, often relying on the intuition and expertise of the designer. To address these challenges, a machine learning (ML) strategy based on the combination of artificial neural network (ANN) and genetic algorithm (GA) is presented. The ANN is trained to model representative scenarios, viz. NFRHT between metamaterials, NFRHT and thermal rectification between nanoparticles. The influence of different problem complexities, i.e. the number of input variables of function to be fitted, on effectiveness of the trained ANN is investigated. Test results show that ANNs can obtain the radiative heat flow and rectification ratio accurately and rapidly. Subsequently, physical parameters for the largest radiative heat flow and rectification ratio are determined by the utilization of GA on the trained ANN, and underlying mechanisms of deterministic optimum are discussed. Our work shows that data-driven ML methods are a powerful tool which offers unprecedented opportunities for future NFRHT research.

Near-field radiative heat transfer (NFRHT) has many promising applications in a variety of fields from electronic devices to renewable energy utilization due to its high efficiency of energy transmission[1–6]. Previous theoretical research mainly focuses on cases of enhancing the radiative heat transfer far beyond the black-body limit (thermal photovoltaics[7–11], thermal imaging[12–14]) and active control of the heat flow (thermal diodes[15,16], transistors[17], and switches[18–20]). Common methods in previous designs of enhancing and controlling heat flow include inducing surface and hyperbolic modes, employing new materials whose dielectric function are sensitive to the temperature, and exploiting asymmetric nanophotonic structures[21–26]. Nevertheless, these methods very often rely on the intuition and expertise of researchers, ultimately limiting the development of structure for desired radiative properties. Additionally, conventional methods of calculating NFRHT, including rigorous coupled-wave analysis (RWCA)[1,27,28] and dyadic green's functions (DGFs)[29,30], are very computationally expensive. Therefore, exploring a more systematic and efficient method to design thermal devices is very imperative.

In recent years, the advancement of machine learning (ML) algorithms and the abundance of open source software may provide alternative ways for researchers to tackle optimization problems in near-field radiative heat transfer. Prompted by ML's attractive advantages, such as identifying multi-dimensional correlations and exploring massive design spaces, thermal-science research has successfully begun to employ ML, thereby bringing fresh perspectives to its conventional problems[31–34]. In the field of thermal radiation, a large body of researchers are developing ML assisted code that can be efficiently used to optimize structures for a specific purpose[35,36]. For example, Ben-Abdallah et al.[37,38] designed the composite structures to control the thermal emission and local density of state based on genetic algorithms. Hu et al.[39] took the power density and system efficiency as the coupling parameters to optimize the Tamm emitter based on Monte Carlo tree search algorithm. Sakurai et al.[40] designed an ultranarrow-band wavelength-selective thermal radiator by combining the electromagnetic field calculation and Bayesian optimization. Seo et al.[41] applied an evolutionary algorithm to find the optimal geometric parameters of solar thermal absorber for the largest solar absorptance. However, past progress on this topic has mainly focused on harnessing solar radiation for power generation, and the characteristic scale of it is in the far-field radiative heat transfer. The more modern and hotter topics about how ML can be effectively applied in NFRHT remains unclear.

In this work, by combining two data-driven ML methods, viz. artificial neural networks (ANNs)[42] and genetic algorithms (GAs), we propose a flowchart for the modeling and optimal design of near-field thermal devices as shown in figure 1. The adopted workflow is enabled by the following innovative points: first, a sampling method based on Latin hypercube sampling (LHS) and sensitivity analysis (SA) is used for the design parameters of the problem to be studied. These sampled points are calculated with accurate NFRHT method so as to build our training datasets. Second, a surrogate ANN model was trained to construct a functional model from an input feature vector to a corresponding output feature vector, which can be used to predict the NFRHT and rectification ratio of corresponding structures. Finally, GA was applied to the surrogate ANN model to identify the optimal solution for the problem, based on emulating biological evolutionary theories[43,44]. Detailed descriptions and settings of ANN and GA for this research can see the supplementary material.

To illustrate these ideas, the proposed workflow has been firstly dedicated to tackling the structural optimization of NFRHT between multilayered metamaterials, which shows unprecedented potentials to manipulate light and heat beyond

[a)]These two authors contributed equally

1.jpg

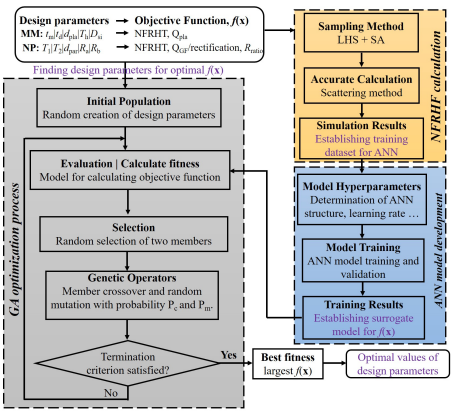

FIG. 1. Outline of proposed machine learning strategy. Goal of this workflow is to model the NFRHT/rectification ratio (objective function) between multilayered metamaterials (MM) and nanoparticles (NP), and decide design parameters for the largest value of objective functions.

substances existing in nature. NFRHT between two periodic multilayered metamaterials configured by doped silicon (D-Si) and germanium (Ge) in Ref. 45 are reconsidered. The system under consideration is shown in figure 2. In the modeling, $t_{\rm m}$ and $t_{\rm d}$ are the thickness of D-Si (metallic behavior) and Ge (dielectric), respectively. The resulting period $P = t_{\rm m} + t_{\rm d}$ is set to 50 so as to approximate a semi-infinite structure. Metal-dielectric (MD) configuration for the two layers adjacent to vacuum is employed. The temperature of each body is assumed to be uniform at $T_{\rm h}$ and $T_{\rm l}$, respectively. The dielectric function of D-Si (n-type) with a doping concentration of $D_{\rm si}$ is obtained from Ref. 46. And the relative permittivity of vacuum and Ge is treated as constants 1 and 16, respectively. NFRHT between two multilayered structures can be described as

$$\mathrm{Q_{pla}} = \frac{1}{4\pi^2}\int_0^\infty [\Theta(\omega,T_1)-\Theta(\omega,T_2)]d\omega \int_0^\infty \beta \times \sum_{\rm j=s,p} \xi_j(\omega,\beta)\,d\beta \tag{1}$$

where $\Theta(\omega,T)$ represents the mean energy of Planck's oscillator, $\xi_j(\omega,\beta)$ is the energy transmission coefficient depending on the reflection coefficient matrix of the structure, j is either s or p for different polarizations. In the present study, scattering theory and effective medium theory (EMT) in Ref. 45 are used to calculate the accurate and approximate value of energy transmission coefficient, respectively.

Usually, when the functional relationship between input $\boldsymbol{\alpha}$ and output $Q_{\rm ANN}$ become more complex, larger training dataset and network architectures are required so as to retain a good prediction performance[47]. To better reflect the applicability of ANN to problems with different complexities, four

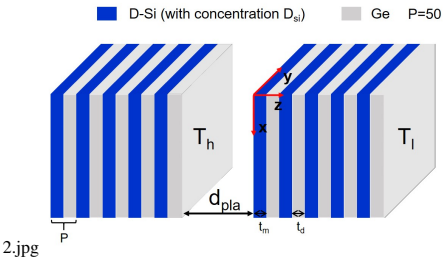

2.jpg

FIG. 2. Schematic of near-field thermal radiation between two multilayered metamaterials (at temperature T_h and T_l, respectively), separated by a vacuum gap $d_{\rm pla}$. The thickness of D-Si with a doping concentration of $D_{\rm si}$ and Ge layers are $t_{\rm m}$ and $t_{\rm d}$, respectively, resulting in a unit cell of period $P = t_{\rm m} + t_{\rm d}$.

TABLE I. Range of considered variables for multilayer metamaterials

Parameter[a]	$t_{\rm m}$	$t_{\rm d}$	$d_{\rm pla}$	$T_{\rm h}$	$D_{\rm si}$
Lower Bound	10	10	10	300	1×10^{18}
Upper Bound	500	500	500	400	1×10^{20}
Default Value			100	300	1×10^{20}

[a] Units for $t_{\rm m}$, $t_{\rm d}$ and $d_{\rm pla}$ are nanometer (nm). Units for $T_{\rm h}$ and $D_{\rm si}$ are Kelvin (K) and cm^{-3}, respectively.

different functional models were considered, including two-input model {input: ($t_{\rm m}$, $t_{\rm d}$), output: $Q_{\rm pla}$}, three-input model {input: ($t_{\rm m}$, $t_{\rm d}$, $d_{\rm pla}$), output: $Q_{\rm pla}$}, four-input model {input: ($t_{\rm m}$, $t_{\rm d}$, $d_{\rm pla}$, $T_{\rm h}$), output: $Q_{\rm pla}$} and five-input model {input: ($t_{\rm m}$, $t_{\rm d}$, $d_{\rm pla}$, $T_{\rm h}$, $D_{\rm si}$), output: $Q_{\rm pla}$}. The range of considered variables for sampling is shown in Table I. Parameters will take the default value if they are not considered as input variables. And the temperature of T_l is taken as 0 K in all cases.

A uniformly distributed sampling method like LHS is firstly used and four different sizes of training datasets without prejudice (1000, 2000, 3000 and 4000) are obtained toward problems with different complexities. However, according to the Ref. 48 and 49. Neural networks are biased towards learning less complex functions, and uniform input data distributions over the parameter space struggle to learn high-gradient components and often fail to train. To address this challenge, non-uniform input data distributions are generated, and more sampled points in high-gradient regions are conducted additionally sampling. We mainly implement the global sensitivity analysis (GSA) to help us identify the essential parameters for the steep variation (gradients), thereby generating our additionally sampled points. Results show that vacuum gap distance $d_{\rm pla}$ is the most influential parameter, aligning with the existing evanescent wave theory in NFRHT. Additional 300 points, 400 points and 500 points for three-input, four-input and five-input model, were sampled in regions with small values of $d_{\rm pla}$. Subsequently, these training datasets and four different ANN architectures are applied to train the model, respectively. More details about sampling methods and training

process can see the supplementary material.

Adjusted coefficient of determination (Adjusted-R^2) are used to characterize the performance of developed model, which can be expressed as follows:

$$R^2 = 1 - \frac{\sum_{i=1}^{n} \left(y_{\text{predict},i} - y_{\text{data},i}\right)^2}{\sum_{i=1}^{n} \left(y_{\text{data},i} - \bar{y}_{\text{data},i}\right)^2} \tag{2a}$$

$$\text{Adjusted} - R^2 = 1 - \frac{\left(1 - R^2\right)(n-1)}{n-k-1} \tag{2b}$$

where $y_{\text{predict},i}$ is the value predicted by ANN at test data point i, $y_{\text{data},i}$ is the actual value calculated by scatter theory at point i, n is the size of the test dataset, and k is the number of input variables for the model. Results of trained models on test dataset (100 points generated by LHS) are shown in Table II. It can be clearly seen that Adjusted-R^2 for four models is approximately 1. This suggests that prediction results of neural network are in good agreement with true values in considered ranges. In figure 3, we show errors of different testing structures predicted by the five-input ANN and EMT. And the error is defined by the following equation:

$$\text{Error} = \left| \frac{Q_{\text{predicted}} - Q_{\text{accurate}}}{Q_{\text{accurate}}} \right| \tag{3}$$

From the results, we can see that only when $d_{\text{pla}}/(t_{\text{m}} + t_{\text{d}})$ is large enough, can EMT be accurate to predict the NFRHT. This aligns with the application conditions of EMT in NFRHT between multilayer metamaterials[45]. In contrast, the ANN model can have relative small errors (less than 5%) in all ranges.

Subsequently, the trained ANN is used as a surrogate model and another ML technique, viz. genetic algorithm, is applied for finding values of input variables for the optimal output. Due to the high efficiency of inference for ANN, the whole optimization process is taken no more than 1 minute, and corresponding results are shown in Table III. To verify the reasonability of results, we calculate the dependence of NFRHT as a function of design parameters using the rigorous scattering method and compare the optimal value with that given by GA. Physically speaking, we only need to look for the optimal t_{m}, t_{d} and D_{si}, because it is obvious to enhance the NFRHT by decreasing vacuum gap distances and improving the temperature difference between emitter and receiver, so as to intensify the evanescent and propagating waves. For two-input, three-input and four-input model, NFRHT as a function of the thickness of D-Si t_{m} and Ge t_{d} are shown in Fig. 4 (a)-(c), respectively. For five-input model, considering the optimal value for t_{d} in all models (two-input, three-input, four-input and five-input)

TABLE II. Adjusted-R^2 results for the ANN model of four different inputs.

Category	Two-input	Three-input	Four-input	Five-input
Adjusted-R^2	1	1	0.9998	0.9996

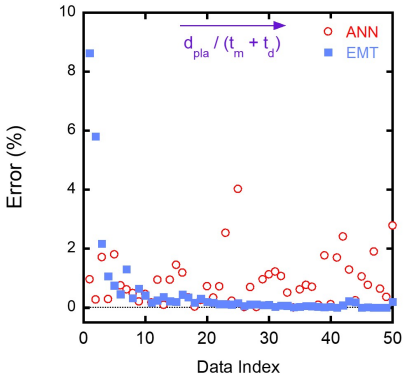

3.jpg

FIG. 3. The errors of different testing structures predicted by ANN and EMT. The testing data sets are randomly generated by LHS. In order to shown the characteristics of EMT, we sort the data by $d_{pla}/(t_m + t_d)$.

is 10 nm, the NFRHT as a function of t_{d} and D_{si} is only shown in Fig. 4(d). Optimal values obtained by scattering methods and GA are represented by blue circle and red pentacle, respectively. Results show that values determined by GA align well with that determined by rigorous scattering method in Fig. 4(a)-(d). For two-input and three-input model, the optimal region for NFRHT corresponds to the lower bound of t_{m} and t_{d} in Table I, which can be attributed to the well excitation of wide-band hyperbolic modes[45]. For four-input and five-input model, inversely, optimal values for t_{m} correspond to the upper bound in Table I. Although there exists a difference in Fig. 4(c), we find that the heat flux saturates and reaches nearly a constant when t_{m} is larger than 100 nm. This is because the whole system can be approximated as the NFRHT between two semi-infinite plates made of silicon with the gap distance equal to 20 nm, given that the dielectric function of Ge is a constant. Therefore, the optimization results of four-input and five-input model for 100 <=t_{m}<=500 is reasonable.

To elucidate the underlying mechanism for the change of optimal t_{m} value, contour plots are generated in Fig. 5 (a)(b) for three and four input cases, to show the dependence of transmission coefficient ξ (equals to $\xi_p + \xi_s$) on the lateral wave vector β and angular frequency ω. Figure 5(b) shows that ξ of four-input model has a much larger contribution around 2.5×10^{14} rad/s mainly caused by the excitation of surface plasmon polaritons (SPPs) at Si-vacuum interface, demonstrated by the SPP dispersion $k_{\text{SPP}} = \omega / c_0 \sqrt{\varepsilon_{\text{D-Si}} / (1 + \varepsilon_{\text{D-Si}})}$. At the same time, figure 5(d) shows that the Planck oscillator energy in high angular frequency will be activated at 400 K. Therefore, it will have a good match with the SPPs, and subsequently a significant increase of spectral heat transfer in the high frequency band will occur, shown in Fig. 5(d). For five-input model, we find that a lower dope concentration will lead to a higher value of

TABLE III. Optimization results for the ANN surrogate model of four different inputs. Numbers in brackets indicate the default value of corresponding parameters. Q_{ANN} is the radiative heat flow predicted by the ANN. Q_{scatter} is the accurate heat flow calculated by scatter theory on the deterministic optimum. Error is defined by the equation 3.

Category[a]	t_{m}	t_{d}	d_{pla}	T_{h}	D_{si}	Q_{ANN}	Q_{scatter}	Error
Two-input	10	10	(100)	(300)	(1×10^{20})	6744	6438	4.75%
Three-input	10	10	10	(300)	(1×10^{20})	191883	197550	2.87%
Four-input	320	10	10	400	(1×10^{20})	666398	623320	6.91%
Five-input	500	10	10	400	1.93×10^{19}	1334861	1391800	4.09%

[a] Units for Q_{ANN} and Q_{scatter} are W/m^2.

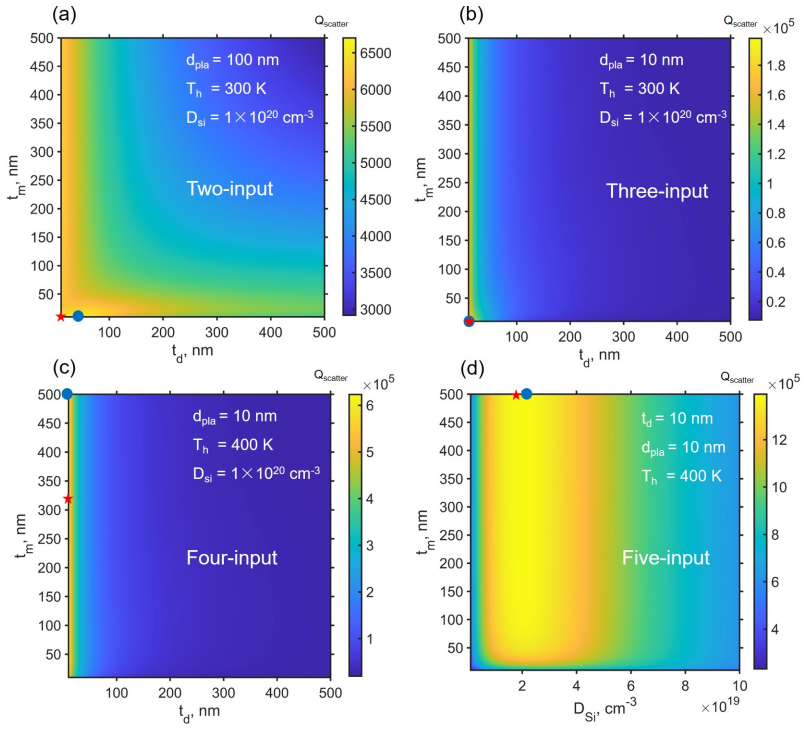

4.jpg

FIG. 4. NFRHT as a function of the thickness of D-Si t_{m} and Ge t_{d} in (a) two-input model; (b) three-input model; (c) four-input model. (d) NFRHT as a function of the thickness of D-Si t_{m} and the doping concentration of D-Si D_{si} in five-input model. The blue circle and red pentacle indicate the maximum NFRHT given by the rigorous scattering method and GA.

the D-Si dielectric function's real part. This means that the ML algorithm can adjust its resonant frequency of the excited mode when the doping of silicon is further listed as the objective for optimization. And results show that GA accurately align its resonant frequency to region for high $\Theta(\omega,T)$ value, which gives rise to the larger enhancement of NFRHT, shown in Fig. 5(c) and (d). Above analysis verify the correctness of deterministic optimum determined by the ANN and GA. It fully demonstrates the great potential of ML methods in the modeling and optimal design of NFRHT.

TABLE IV. Estimated time of the proposed workflow for the design of multilayered metamaterials.

Process	Accurate calculation	Model training	GA optimization
cost	3.4 hours/1000 points	∼10 minutes	∼30 seconds

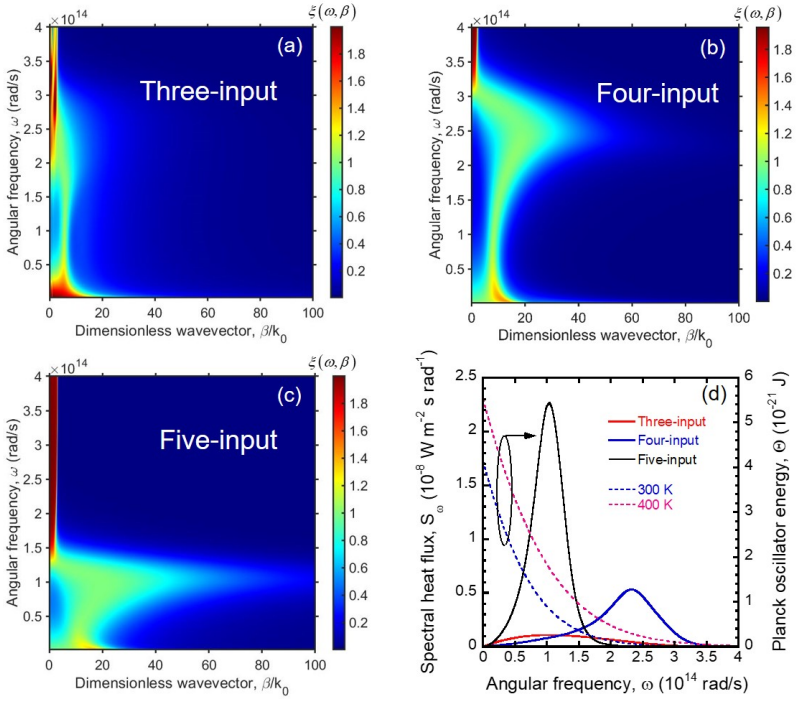

5.jpg

FIG. 5. Transmission coefficient contours $\xi(\omega,\beta)$ of the deterministic optimum for (a) three-input model; (b) four-input model; (c) five-input model. Corresponding spectral heat flux and Planck oscillator energy are shown in (d).

To illustrate the efficiency of our proposed ML method, the estimated time of each part in Fig. 1 for the design of multi-layered metamaterials are listed in Table IV. In our workstation (Xeon E5-2697 v4), the consumed time for calculating 1000 points based on scattering methods is 3.4 hours. Because we apply the second-order optimization algorithm, the rate of convergence for training ANN model is very fast and the consumed time is less than 10 minutes. After building the surrogate model, it only takes 30 seconds for GA to find the optimal design. In comparison, parametric analysis methods based on rigorous scattering method is time consuming. For example, 2500 points are calculated to draw the 50×50 contour plot in Fig. 4, with only considering two variables.

TABLE V. Range of considered variables for nanoparticles

Parameter[a]	T_1	T_2	d_{par}	R_a	R_b
Lower Bound	200	200	10	100	10
Upper Bound	1000	1000	200	200	50

[a] Units for T_1 and T_2 are Kelvin (K). Units for d_{par}, R_a and R_b are nanometer (nm).

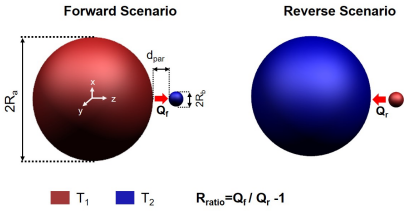

6.jpg

FIG. 6. Schematic diagram of NFRHT and thermal rectification between two nanospheres made of 3C-SiC separated by a vacuum gap d_{par}. R_a and R_b represent the radius of sphere a and sphere b. T_1 and T_2 are set as the temperature of emitter and receiver, respectively.

When considering five variables, conventional methods will take huge computational cost and is nearly impossible. We need to also mention that the training process is not fully optimized. There is still space to improve the speed and accuracy.

In order to verify the applicability of our proposed workflow in different structures and issues, another important categories in the near-field regime, viz. NFRHT and rectification

TABLE VI. Optimization results of trained ANN models for radiative heat flow and rectification ratio between nanoparticles.

Category[a]	T_1	T_2	d_{par}	R_a	R_b	Q_{ANN}	Q_{GF}	Error
Radiative heat flow	1000	506	10	200	50	27.96	27.81	0.5%
Rectification ratio	696	200	27.5	200	10	8.48	8.44	0.391%

[a] Units for Q_{ANN}, Q_{GF} are nW.

ratio between nanoparticles, are further considered. In this paper, we consider the configuration of two nanospheres made of the same polytype of 3C-SiC[50]. The accurate NFRHT between two spheres can be derived by using dyadic Green's functions (DGFs) and the fluctuation-dissipation theorem, which is described in detail in Ref. 30. The performance of rectifiers can be characterized by the thermal rectification ratio as

$$R_{ratio} = \frac{Q_f - Q_r}{Q_r} \tag{4}$$

where Q_f and Q_r are the net heat fluxes in the forward and reverse scenarios, respectively. Shown in figure 6, for the forward scenario, 3C-SiC with radius R_a is the emitter at the temperature of T_1, and the receiver 3C-SiC is maintained at T_2. For the reverse scenario, temperatures of two spheres are switched, and the reverse NFRHT is Q_r. Gap distances for both scenarios are d_{par}.

Here, we only discuss the most complex condition, five-input model. The range of considered variables for sampling is shown in Table V. Training details of ANN are in the supplementary material. Deterministic parameters for the largest NFRHT and rectification ratio are shown in Table VI. We can see that trained ANNs is accurate enough for predicting the value of deterministic optimum of nanoparticles and errors between predicted values and accurate ones is no more than 1%. The deterministic parameters align well with results in Ref.[50], which did lots of parametric analysis and calculations. This also demonstrates that proposed workflow has great advantages in terms of the applicability in different issues and huge computational reduction.

To summary, by utilizing two mainstream ML algorithm, viz. ANN and GA, we report a systematic workflow for modeling and optimal design of NFRHT. Through applying it to representative scenarios including NFRHT between multilayer metamaterials, NFRHT and thermal rectification between nanoparticles, we fully demonstrates its huge computational reduction and wide applicability in different NFRHT research. These advantages is believed to have great potentials in future scientific research and industrial production. Next, better sampling methods and more advanced machine learning algorithms such as convolutional/recurrent/graph neural networks in NFRHT can be further explored. Spectral radiative heat transfer of arbitrary structures and materials is expected for modeling so as to better conduct the inverse design of the system.

SUPPLEMENTARY MATERIAL

See the supplementary material for detailed introduction of ML strategy, training process of ANNs.

This work is mainly supported by China National Key Research and Development Plan Project (Nos. 2018YFB1502000 and 2018YFA0702300) and National Natural Science Foundation of China (Nos. 51706096 and 51820105010). XL also wants to thank the support by the Fundamental Research Funds for the Central Universities (No. 56XIA17001).

DATA AVAILABILITY

The data that support the findings of this study are available from the corresponding author upon reasonable request.

REFERENCES

[1] X. Liu, L. Wang, and Z. M. Zhang, "Near-field thermal radiation: recent progress and outlook," Nanoscale and Microscale Thermophysical Engineering **19**, 98–126 (2015).
[2] S.-A. Biehs, R. Messina, P. S. Venkataram, A. W. Rodriguez, J. C. Cuevas, and P. Ben-Abdallah, "Near-field radiative heat transfer in many-body systems," Reviews of Modern Physics **93**, 025009 (2021).
[3] W. Li and S. Fan, "Nanophotonic control of thermal radiation for energy applications," Optics express **26**, 15995–16021 (2018).
[4] C. Lucchesi, R. Vaillon, and P.-O. Chapuis, "Radiative heat transfer at the nanoscale: experimental trends and challenges," Nanoscale Horizons **6**, 201–208 (2021).
[5] E. Tervo, E. Bagherisereshki, and Z. Zhang, "Near-field radiative thermoelectric energy converters: a review," Frontiers in Energy **12**, 5–21 (2018).
[6] S. Molesky, P. S. Venkataram, W. Jin, and A. W. Rodriguez, "Fundamental limits to radiative heat transfer: Theory," Physical Review B **101**, 035408 (2020).
[7] C. Dang, X. Liu, H. Xia, S. Wen, and Q. Xu, "High-performance three-body near-field thermophotovoltaic energy conversion," Journal of Quantitative Spectroscopy and Radiative Transfer **259**, 107411 (2021).
[8] R. Mittapally, B. Lee, L. Zhu, A. Reihani, J. W. Lim, D. Fan, S. R. Forrest, P. Reddy, and E. Meyhofer, "Near-field thermophotovoltaics for efficient heat to electricity conversion at high power density," Nature communications **12**, 1–8 (2021).
[9] A. Fiorino, L. Zhu, D. Thompson, R. Mittapally, P. Reddy, and E. Meyhofer, "Nanogap near-field thermophotovoltaics," Nature nanotechnology **13**, 806–811 (2018).
[10] B. Zhao, P. Santhanam, K. Chen, S. Buddhiraju, and S. Fan, "Near-field thermophotonic systems for low-grade waste-heat recovery," Nano letters **18**, 5224–5230 (2018).
[11] S. Hassan, C. F. Doiron, and G. V. Naik, "Optimum selective emitters for efficient thermophotovoltaic conversion," Applied Physics Letters **116**, 023903 (2020).

[12]A. Kittel, W. Müller-Hirsch, J. Parisi, S.-A. Biehs, D. Reddig, and M. Holthaus, "Near-field heat transfer in a scanning thermal microscope," Physical review letters **95**, 224301 (2005).
[13]A. Kittel, U. F. Wischnath, J. Welker, O. Huth, F. Rueting, and S.-A. Biehs, "Near-field thermal imaging of nanostructured surfaces," Applied Physics Letters **93**, 193109 (2008).
[14]Y. De Wilde, F. Formanek, R. Carminati, B. Gralak, P.-A. Lemoine, K. Joulain, J.-P. Mulet, Y. Chen, and J.-J. Greffet, "Thermal radiation scanning tunnelling microscopy," Nature **444**, 740–743 (2006).
[15]M. Wong, C. Tso, T. Ho, and H. Lee, "A review of state of the art thermal diodes and their potential applications," International Journal of Heat and Mass Transfer **164**, 120607 (2021).
[16]S. Wen, X. Liu, S. Cheng, Z. Wang, S. Zhang, and C. Dang, "Ultrahigh thermal rectification based on near-field thermal radiation between dissimilar nanoparticles," Journal of Quantitative Spectroscopy and Radiative Transfer **234**, 1–9 (2019).
[17]P. Ben-Abdallah and S.-A. Biehs, "Near-field thermal transistor," Physical review letters **112**, 044301 (2014).
[18]X. Liu, J. Shen, and Y. Xuan, "Pattern-free thermal modulator via thermal radiation between van der waals materials," Journal of Quantitative Spectroscopy and Radiative Transfer **200**, 100–107 (2017).
[19]F. Chen, X. Liu, Y. Tian, Y. Liu, and Y. Zheng, "Self-adaptive near-field radiative thermal modulation using a thermally sensitive bimaterial structure," Applied Physics Letters **119**, 221107 (2021).
[20]W. Gu, G.-H. Tang, and W.-Q. Tao, "Thermal switch and thermal rectification enabled by near-field radiative heat transfer between three slabs," International Journal of Heat and Mass Transfer **82**, 429–434 (2015).
[21]J. Shen, X. Liu, H. He, W. Wu, and B. Liu, "High-performance noncontact thermal diode via asymmetric nanostructures," Journal of Quantitative Spectroscopy and Radiative Transfer **211**, 1–8 (2018).
[22]Y. Kan, C. Zhao, and Z. Zhang, "Near-field radiative heat transfer in three-body systems with periodic structures," Physical Review B **99**, 035433 (2019).
[23]K. Ito, K. Nishikawa, A. Miura, H. Toshiyoshi, and H. Iizuka, "Dynamic modulation of radiative heat transfer beyond the blackbody limit," Nano letters **17**, 4347–4353 (2017).
[24]X. Wu and C. Fu, "Near-field radiative modulator based on dissimilar hyperbolic materials with in-plane anisotropy," International Journal of Heat and Mass Transfer **168**, 120908 (2021).
[25]X. Liu and Y. Xuan, "Near-field thermal radiation of metamaterials/metasurfaces constructed of natural anisotropic materials," Annual Review of Heat Transfer **23** (2020).
[26]D. Xu, J. Zhao, and L. Liu, "Near-field thermal radiation of gradient refractive index slab: Internal polaritons," Applied Physics Letters **119**, 141106 (2021).
[27]J. Dai, F. Ding, S. I. Bozhevolnyi, and M. Yan, "Ultrabroadband superplanckian radiative heat transfer with artificial continuum cavity states in patterned hyperbolic metamaterials," Physical Review B **95**, 245405 (2017).
[28]Y. Kan and C. Zhao, "Near field radiative heat transfer in asymmetric three-grating systems," International Journal of Heat and Mass Transfer **171**, 121124 (2021).
[29]A. Narayanaswamy and Y. Zheng, "A green's function formalism of energy and momentum transfer in fluctuational electrodynamics," Journal of Quantitative Spectroscopy and Radiative Transfer **132**, 12–21 (2014).
[30]A. Narayanaswamy and G. Chen, "Thermal near-field radiative transfer between two spheres," Physical Review B **77**, 075125 (2008).
[31]R. Li, Z. Liu, A. Rohskopf, K. Gordiz, A. Henry, E. Lee, and T. Luo, "A deep neural network interatomic potential for studying thermal conductivity of β-ga2o3," Applied Physics Letters **117**, 152102 (2020).
[32]X. Wan, W. Feng, Y. Wang, H. Wang, X. Zhang, C. Deng, and N. Yang, "Materials discovery and properties prediction in thermal transport via materials informatics: a mini review," Nano letters **19**, 3387–3395 (2019).
[33]T. Wang, C. Zhang, H. Snoussi, and G. Zhang, "Machine learning approaches for thermoelectric materials research," Advanced Functional Materials **30**, 1906041 (2020).
[34]D. Visaria and A. Jain, "Machine-learning-assisted space-transformation accelerates discovery of high thermal conductivity alloys," Applied Physics Letters **117**, 202107 (2020).
[35]J. J. García-Esteban, J. Bravo-Abad, and J. C. Cuevas, "Deep learning for the modeling and inverse design of radiative heat transfer," Physical Review Applied **16**, 064006 (2021).
[36]W. Zhang, B. Wang, and C. Zhao, "Selective thermophotovoltaic emitter with aperiodic multilayer structures designed by machine learning," ACS Applied Energy Materials **4**, 2004–2013 (2021).
[37]P. Ben-Abdallah, K. Joulain, J. Drevillon, and G. Domingues, "Tailoring the local density of states of nonradiative field at the surface of nanolayered materials," Applied Physics Letters **94**, 153117 (2009).
[38]J. Drevillon and P. Ben-Abdallah, "Ab initio design of coherent thermal sources," Journal of Applied Physics **102**, 114305 (2007).
[39]R. Hu, J. Song, Y. Liu, W. Xi, Y. Zhao, X. Yu, Q. Cheng, G. Tao, and X. Luo, "Machine learning-optimized tamm emitter for high-performance thermophotovoltaic system with detailed balance analysis," Nano Energy **72**, 104687 (2020).
[40]A. Sakurai, K. Yada, T. Simomura, S. Ju, M. Kashiwagi, H. Okada, T. Nagao, K. Tsuda, and J. Shiomi, "Ultranarrow-band wavelength-selective thermal emission with aperiodic multilayered metamaterials designed by bayesian optimization," ACS central science **5**, 319–326 (2019).
[41]J. Seo, P.-H. Jung, M. Kim, S. Yang, I. Lee, J. Lee, H. Lee, and B. J. Lee, "Design of a broadband solar thermal absorber using a deep neural network and experimental demonstration of its performance," Scientific reports **9**, 1–9 (2019).
[42]D. E. Rumelhart, J. L. McClelland, P. R. Group, *et al.*, *Parallel distributed processing*, Vol. 1 (IEEE New York, 1988).
[43]K. Höschel and V. Lakshminarayanan, "Genetic algorithms for lens design: a review," Journal of Optics **48**, 134–144 (2019).
[44]M. A. Albadr, S. Tiun, M. Ayob, and F. Al-Dhief, "Genetic algorithm based on natural selection theory for optimization problems," Symmetry **12**, 1758 (2020).
[45]X. Liu, T. Bright, and Z. Zhang, "Application conditions of effective medium theory in near-field radiative heat transfer between multilayered metamaterials," Journal of Heat Transfer **136** (2014).
[46]S. Basu, B. J. Lee, and Z. Zhang, "Infrared radiative properties of heavily doped silicon at room temperature," (2010).
[47]M. T. Hagan, H. B. Demuth, and M. Beale, *Neural network design* (PWS Publishing Co., 1997).
[48]G. E. Karniadakis, I. G. Kevrekidis, L. Lu, P. Perdikaris, S. Wang, and L. Yang, "Physics-informed machine learning," Nature Reviews Physics **3**, 422–440 (2021).
[49]Y. Cao, Z. Fang, Y. Wu, D.-X. Zhou, and Q. Gu, "Towards understanding the spectral bias of deep learning," in *30th International Joint Conference on Artificial Intelligence (IJCAI 2021)* (International Joint Conferences on Artificial Intelligence, 2021) pp. 2205–2211.
[50]L. Zhu, C. R. Otey, and S. Fan, "Ultrahigh-contrast and large-bandwidth thermal rectification in near-field electromagnetic thermal transfer between nanoparticles," Physical Review B **88**, 184301 (2013).